Chinese Chemical Letters 33 (2022) 3053–3060

Contents lists available at ScienceDirect

Chinese Chemical Letters

journal homepage: www.elsevier.com/locate/cclet

Design of $BiOBr_{0.25}I_{0.75}$ for synergy photoreduction Cr(VI) and capture Cr(III) over wide pH range

Lixia Jia[a], Xin Tan[a,d], Yanfang Li[a], Yizhong Zhang[a], Shiqian Cao[c], Wei Zhou[c,*], Xiang Huang[d], Lequan Liu[e], Tao Yu[b,*]

[a] School of Environmental Science and Engineering, Tianjin University, Tianjin 300350, China
[b] School of Chemical Engineering and Technology, Tianjin University, Tianjin 300350, China
[c] School of Science, Tianjin University, Tianjin 300350, China
[d] School of Science, Tibet University, Lhasa 850000, China
[e] School of Materials Science and Engineering, Tianjin University, Tianjin 300350, China

ARTICLE INFO

Article history:
Received 12 July 2021
Revised 12 August 2021
Accepted 13 September 2021
Available online 17 September 2021

Keywords:
Adsorption
Photoreduction
$BiOBr_{0.25}I_{0.75}$
Chromium

ABSTRACT

Conversion of hexavalent chromium (Cr(VI)) to trivalent chromium (Cr(III)) is an effective way to reduce its environmental risk, especially *via* photoreduction process. However, over a wide range of pH values, it is still a great challenge to achieve a high removal rate, and the disposal of produced Cr(III) should be concerned. In this work, we implemented a high removal rate at 98% for Cr(VI) and total chromium (Cr(T)) over a wide pH range (4–10) through the synergistic effect of adsorption, photoreduction and immobilization on the surface of $BiOBr_{0.25}I_{0.75}$. The substitution of bromine by iodine reduced the adsorption energy of Cr(VI) on $BiOBr_{0.25}I_{0.75}$, promoting the adsorption of Cr(VI). Meanwhile, the introduced iodine upshifted the conduction band (CB), enhancing the reduction ability for Cr(VI) to Cr(III). The negative surface of $BiOBr_{0.25}I_{0.75}$ can capture Cr(III), achieving a high removal rate for Cr(T). The pH-independent feature for Cr(VI) and Cr(III) removal make $BiOBr_{0.25}I_{0.75}$ a potential material for chromium-containing wastewater treatment. This work provides an effective strategy for removing chromium over a wide pH range.

Hexavalent chromium (Cr(VI)), generated from leather tanning, paint production and electroplating, has attracted more attention for its high solubility, mobility, and carcinogenicity [1–5]. Photoreduction Cr(VI) to trivalent chromium (Cr(III)) exhibits great advantages regarding its lower energy consumption, higher efficiency and lower toxicity of Cr(III) [6–10]. However, the drawback of photoreduction is that it can only be realized under acidic conditions. The removal of Cr(VI) under neutral and alkaline conditions is still a challenge, and immobilization of Cr(III) generated by photoreduction process should be paid attention due to its potential hazards.

Previous researches have reported on the photoreduction of Cr(VI) under acidic conditions, which exhibits an efficient removal rate [11–13]. Wang *et al.* [14] achieved the efficient removal of Cr(VI) by amine-CdS/MoO_3 at pH 2 through the synergy of adsorption and photoreduction, but the efficiency decreased significantly at pH 4. Yuan *et al.* [15] reported highly efficient sunlight-driven reduction of Cr(VI) by TiO_2@NH_2-MIL-88B (Fe) heterostructures at pH 7, resulting from the high photoelectron-hole separation and migration efficiency. Consider that the combination of adsorption and photocatalytic reaction could avoid treating trace level pollutants and benefit its application [16], researchers also took into the immobilization of Cr(III) after photoreduction process. Liu *et al.* [17] reported the simultaneous removal of Cr(VI) and Cr(III) with TiO_2 and titanate nanotubes at pH 5, in which TiO_2 acted as photocatalyst and titanate nanotubes can adsorbed Cr(III) after photoreduction. Li *et al.* [18] realized the highest concurrent photoreduction Cr(VI) and adsorption Cr(III) by Mn_3O_4@ZnO/Mn_3O_4 at pH 6, with the synergy photocatalysis on Mn_3O_4@ZnO and adsorption on Mn_3O_4. Nevertheless, the researches for Cr(VI) removal and Cr(III) capture under alkaline conditions are barely reported, and the relationship between pH and chromium removal has not been systematically studied. It is urgent to seek a material that can remove chromium within a wide pH range.

Recently, several researches have demonstrated that BiOBr exhibits favorable photoreduction from Cr(VI) to Cr(III) in acidic conditions [19–23]. As a layer structured semiconductor, BiOBr has been paid more attention for its visible light response, satisfactory optical properties and high chemical stability [24–26]. Shang

* Corresponding authors.
E-mail addresses: weizhou@tju.edu.cn (W. Zhou), yutao@tju.edu.cn (T. Yu).

https://doi.org/10.1016/j.cclet.2021.09.043
1001-8417/

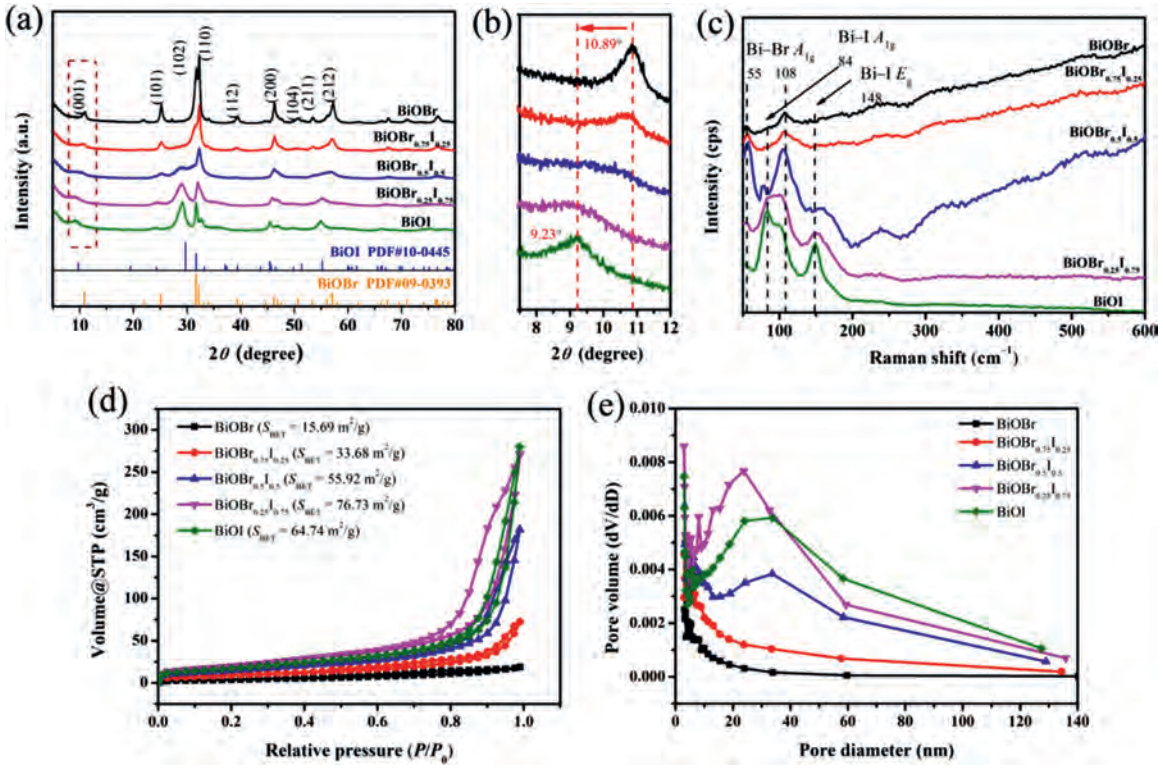

Fig. 1. (a) XRD patterns of $BiOBr_{1-x}I_x$. (b) Zoomed-in view of XRD patterns at 2θ = 8°–12°. (c) Raman spectra of $BiOBr_{1-x}I_x$. (d) N_2 adsorption-desorption isotherms and (e) the corresponding pore size distribution of $BiOBr_{1-x}I_x$.

et al. [27] reported the enhanced photocatalytic reduction of Cr(VI) at pH 2 with $Bi_{24}O_{31}Br_{10}$, which is caused by the variation of Bi 6p and Br 4s orbitals hybridization and uplifting of the conduction band (CB). By ion exchange and Z-scheme heterojunction construction, Long *et al.* [28] prepared BiOBr-Bi_2S_3 with high photoreduction performance for Cr(VI), and the contribution of adsorption plays an important role in the removal of Cr(VI). Based on our recent research, BiOBr can realize enhanced adsorption of Cr(VI) under neutral and alkaline conditions through anion exchange. Meanwhile, the zeta potential of BiOBr is negative at pH 2 to 12, which will facilitate the adsorption of positively charged ions through electrostatic attraction [29]. These indicate that BiOBr is expected to remove both Cr(VI) and Cr(III) within a wide pH range *via* the synergy of adsorption and photoreduction.

In this study, by introducing iodine into BiOBr, we devised a series of solid solution $BiOBr_{1-x}I_x$ by a solvothermal method. The molar ratio of Br/I was regulated to achieve the higher specific surface area, the lower adsorption energy of Cr(VI) on $BiOBr_{1-x}I_x$, and more efficient electrons and holes transport. X-ray diffraction (XRD), N_2 adsorption-desorption isotherms, X-ray photoelectron spectroscopy (XPS), electrochemical test and DFT calculation were used to illustrate the variation of crystal structure and energy band structure. The experiments for both Cr(VI) and Cr(III) removal efficiency were conducted in a wide pH range, and the mechanism was proposed accordingly.

The crystal structure is very important information for layered materials prepared in this work. Different crystals will provide different active sites, which determines the performance of adsorption and conversion. Here, the crystalline phases of materials were determined by XRD as was shown in Fig. 1a. The BiOBr sample is well indexed to tetragonal BiOBr (JCPDS PDF #09-0393) with characteristic peaks at 2θ = 10.9°, 25.2°, 31.7° and 32.2°, which corresponds to the (001), (101), (102) and (110) plane, respectively [21,30]. With the percentage of introduced iodine increases, the typical peaks of BiOBr shift to a lower 2θ value, which can be seen clearly in Fig. 1b. The introduction of iodine causes lattice distortion of BiOBr, which changes the lattice parameters and causes the shift of diffraction peaks. Fig. 1c shows the Raman spectra of $BiOBr_{1-x}I_x$. For pure BiOBr, the signals at 55 cm^{-1} and 108 cm^{-1} are assigned to the A_{1g} internal Bi–Br stretching mode [31]. After iodine introducing, the signals for Bi–Br disappear gradually. Two new peaks at around 84 cm^{-1} and 148 cm^{-1} are observed, which are corresponded to A_{1g} and E_g internal Bi–I stretching modes, respectively [32], indicating the existence of iodine in $BiOBr_{1-x}I_x$ and the interaction of Bi and I. The peaks shift in XRD and Raman indicate the successful formation of solid solution $BiOBr_{1-x}I_x$.

Introducing iodine also contributes to the variation of specific surface area and pore size. Figs. 1d and e show the N_2 adsorption-desorption isotherms and the corresponding pore size distribution of $BiOBr_{1-x}I_x$. All the materials show type IV isotherms with H3 hysteresis loop, indicating the pile of nanosheets. With the percentage increase of iodine introducing, the specific surface areas of the materials increase from 15.69 m^2/g (BiOBr) to 76.73 m^2/g ($BiOBr_{0.25}I_{0.75}$). And more mesoporous can be observed for solid solution $BiOBr_{1-x}I_x$. The higher specific surface area and more mesoporous will give more chance for the interaction of materials and Cr(VI), which is beneficial to adsorption and photoreduction.

Fig. 2 shows the scanning electron microscopy (SEM) and high-resolution transmission electron microscopy (HRTEM) images of BiOBr, $BiOBr_{0.25}I_{0.75}$ and BiOI. From SEM images we can see that all the samples are composed of nanosheets for their unique layered structure. For BiOBr, a microsphere composed of thick and dense nanosheets with a diameter of 4.3 μm can be observed (Fig. 2a). The spherical structure is destroyed for solid solution $BiOBr_{1-x}I_x$, instead, plenty of nanosheets stacks irregularly in $BiOBr_{0.25}I_{0.75}$ and BiOI (Figs. 2b and c). According to the magnified images in Figs. 2d-f, compared with BiOBr, the nanosheets in $BiOBr_{0.25}I_{0.75}$ and BiOI are loosely packed, indicating the high specific surface ar-

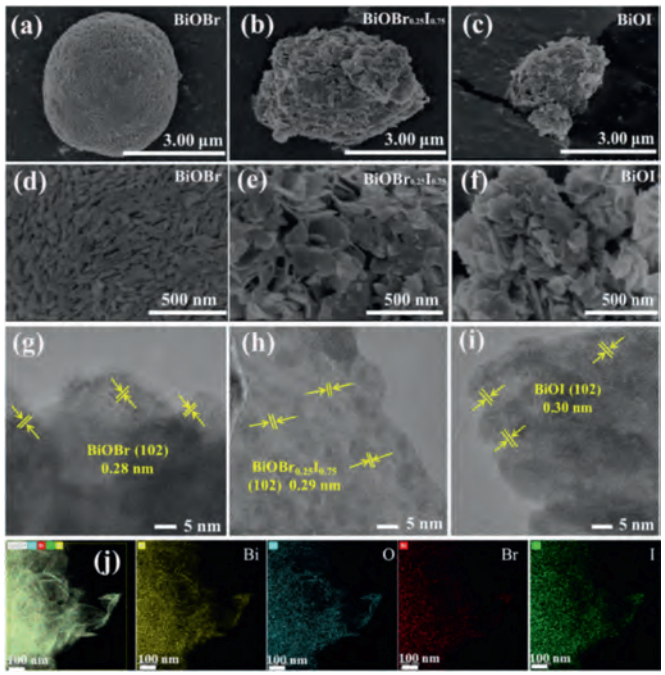

Fig. 2. SEM images of BiOBr (a, d), $BiOBr_{0.25}I_{0.75}$ (b, e), and BiOI (c, f). HRTEM images of BiOBr (g), $BiOBr_{0.25}I_{0.75}$ (h), and BiOI (i). (j) EDS mapping of $BiOBr_{0.25}I_{0.75}$.

eas and more exposed active sites, which is in accordance with N_2 adsorption-desorption isotherms results.

HRTEM was conducted to study the changes of lattice fringes of BiOBr, $BiOBr_{0.25}I_{0.75}$ and BiOI (Figs. 2g-i). The lattice fringes for BiOBr, $BiOBr_{0.25}I_{0.75}$ and BiOI are 0.28 nm, 0.29 nm and 0.30 nm, respectively, which can be indexed into (102) crystal plane. The energy disperse spectroscopy (EDS) mapping of $BiOBr_{0.25}I_{0.75}$ elucidates the homogeneous distribution of Bi, O, Br and I (Fig. 2j).

As we know, the CB of BiOBr is contributed by Bi 6p, O 2p and Br 4p orbits, and the valance band (VB) mainly consists of Br 4p and O 2p orbits [33,34]. The introduction of iodine will decrease the contribution of Br 4p orbit and increase the contribution of I 5p orbit, thus regulate the electronic and band structure of BiOBr. Fig. 3a shows the ultraviolet–visible (UV–vis) reflectance absorption spectra of $BiOBr_{1-x}I_x$ samples. With the increasing percentage of iodine, the absorption edge red shifts from 400 nm to 500 nm, indicating the enhanced light absorption for $BiOBr_{1-x}I_x$. To determine the VB and CB of BiOBr, $BiOBr_{0.25}I_{0.75}$ and BiOI, the XPS spectra and Mott–Schottky plots were conducted. Fig. 3b shows the VB position of BiOBr, $BiOBr_{0.25}I_{0.75}$ and BiOI are 1.77 eV, 1.62 eV, 1.36 eV. The flat band potential of BiOBr, $BiOBr_{0.25}I_{0.75}$ and BiOI can be obtained by Mott-Schottky tests (Fig. 3c). The flat band potential (E_{fb}) of BiOBr, $BiOBr_{0.25}I_{0.75}$ and BiOI are −0.74 eV, −0.83 eV, −1.01 eV versus the saturated calomel electrode (SCE). The positive value indicates that BiOBr, $BiOBr_{0.25}I_{0.75}$ and BiOI are n-type semiconductors [20,35,36]. E_{fb} is equal to Fermi level (E_f), and the potential of CB is more negative by ~ −0.2 eV than E_f. Thus, the corresponding CB potentials of BiOBr, $BiOBr_{0.25}I_{0.75}$ and BiOI are −0.70 eV, −0.79 eV and −0.97 eV versus normal hydrogen electrodes. According to the VB and CB, Fig. 3d illustrates the schematic band positions of $BiOBr_{1-x}I_x$. The introduction of iodine uplifts the VB and CB, promoting the visible light absorption and enhances the reduction ability.

The different electronegativity of bromine and iodine will changes the electron cloud density, leading to binding energy shift of solid solution $BiOBr_{1-x}I_x$. XPS analyses were performed to explore the chemical states and binding energy of the materials. The signals of Bi, O, Br and I are detected in the survey spectra of BiOBr, BiOI, and $BiOBr_{0.25}I_{0.75}$, respectively (Fig. 4a). To clearly explore the chemical states and binding energy, the high-resolution XPS spectra of Br 3d, Bi 4f and O 1s are shown in Figs. 4b-d. For BiOBr, the Br 3d can be divided into two peaks at 68.1 eV and 69.1 eV, which are assigned to Br $3d_{5/2}$ and Br $3d_{3/2}$ [37,38]. A shift of 0.3 eV to high binding energy can be observed for $BiOBr_{0.25}I_{0.75}$, which is caused by interaction of Br and I. The electronegativity of iodine is weaker than that of bromine. Introducing iodine will cause the decrease of electron cloud density around Br, leading to the shift to high binding energy. The Bi 4f spectrum of BiOBr displays a pair of peaks at 159.1 eV and 164.4 eV, corresponding to Bi $4f_{7/2}$ and Bi $4f_{5/2}$ of Bi^{3+} [39,40]. For $BiOBr_{0.25}I_{0.75}$ and BiOI, the peaks have a shift of 0.1–0.2 eV to high binding energy.

The O 1s peak can be divided into three peaks at 529.7 eV, 531.1 eV and 532.5 eV in BiOBr. The first two peaks are lattice oxygen and structural water, respectively, and the third one corresponds to the presence of oxygen vacancies [41]. The oxygen-terminated crystal surface easily reacts with ethylene glycol, leaving some oxygen vacancies on the surface of BiOBr [42,43]. For solid solution $BiOBr_{0.25}I_{0.75}$, the signal for oxygen vacancy disappears. The emergence of iodine may prohibit the reaction between oxygen-terminated and ethylene glycol, reducing the formation of oxygen vacancy. The result is in accordance with electron spin-paramagnetic resonance (ESR) (Fig. S1 in Supporting information) [44,45].

The performance of the samples was evaluated by adsorption and photoreduction Cr(VI). Considering the effect of pH on Cr(VI) removal, the experiments were conducted at pH 2, 3, 5, 7 and 9. Fig. S2 (Supporting information) shows photoreduction of Cr(VI) by $BiOBr_{1-x}I_x$ at pH 2 and pH 3. Among all the materials, $BiOBr_{0.25}I_{0.75}$ shows the highest for Cr(VI), and exceeds most photocatalysts in previous research. It is not surprising for efficient removal of Cr(VI) at pH 2 and 3. In our work, we paid more attention to Cr(VI) removal in a wide pH range (pH 4 to 10). In Fig. 5a, at pH 5, the materials show different adsorption capacities in dark condition. During adsorption process, Cr(VI) concentration decreases slightly with BiOBr, whereas nearly 60% Cr(VI) are removed with $BiOBr_{0.25}I_{0.75}$. With light irradiation, 99% Cr(VI) can be removed with $BiOBr_{0.25}I_{0.75}$ in 60 min, while BiOBr can only remove 44% Cr(VI) in the same time, indicating the enhanced adsorption and photoreduction efficiency for Cr(VI) by solid solution $BiOBr_{0.25}I_{0.75}$. At pH 7 and 9 Figs. 5b and c), the adsorption capacities increase obviously, while the photoreduction efficiency decreases. The mechanism for the enhancement of adsorption capacity will be discussed in the next part. The decrease of photoreduction efficiency is due to the different species of Cr(VI) under acidic conditions and basic conditions, leading to different reduction reactions. Under acidic conditions, $Cr_2O_7^{2-}$ and $HCrO_4^-$ are the main species, and they can be easily reduced to Cr(III) according to Eqs. 1 and 2 [1,2,46]. Under neutral and basic conditions, CrO_4^{2-} is the dominate specie. The reduction reaction is according to Eq. 3. The decreased reduction efficiency for Cr(VI) is caused by the decrease of reduction potential and the formed $Cr(OH)_3$ precipitation, which will seal the active site [46–48]. Though the opposite tendency of adsorption and photoreduction performance at different pH values, the removal rate of Cr(VI) maintains 98% at pH 2 to 10 (Fig. 5e), indicating the favorable synergistic effect of adsorption and photoreduction for Cr(VI).

$$14H^+ + Cr_2O_7^{2-} + 6e^- \rightarrow 2Cr^{3+} + 7H_2O \quad (1)$$

$$7H^+ + HCrO_4^- + 3e^- \rightarrow Cr^{3+} + 4H_2O \quad (2)$$

$$CrO_4^{2-} + 4H_2O + 3e^- \rightarrow Cr(OH)_3(s) + 5OH^- \quad (3)$$

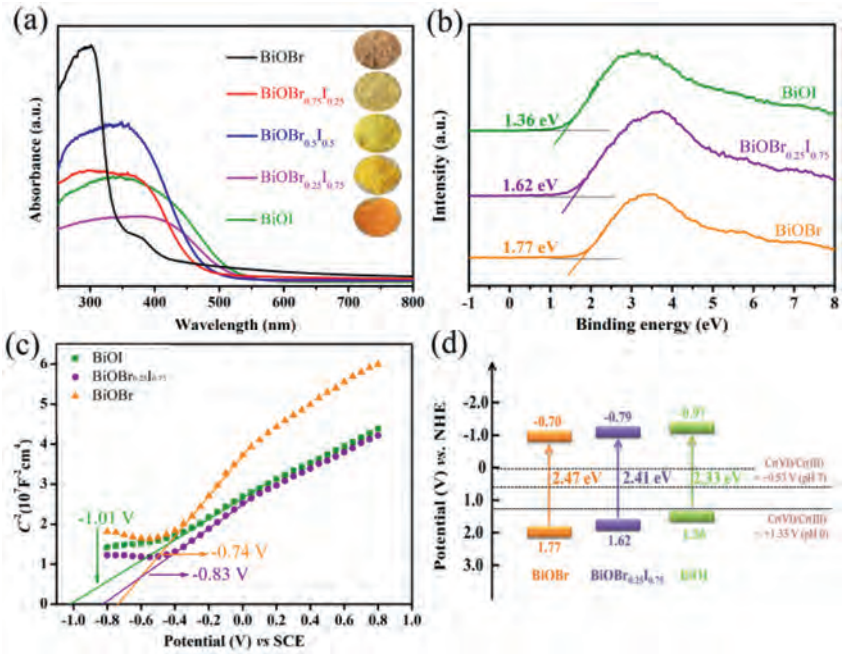

Fig. 3. (a) UV–vis diffuses reflectance spectra of $BiOBr_{1-x}I_x$. (b) XPS-VB spectra and (c) Mott-Schottky spectra of BiOBr, $BiOBr_{0.25}I_{0.75}$ and BiOI. (d) Energy band structure of $BiOBr_{1-x}I_x$.

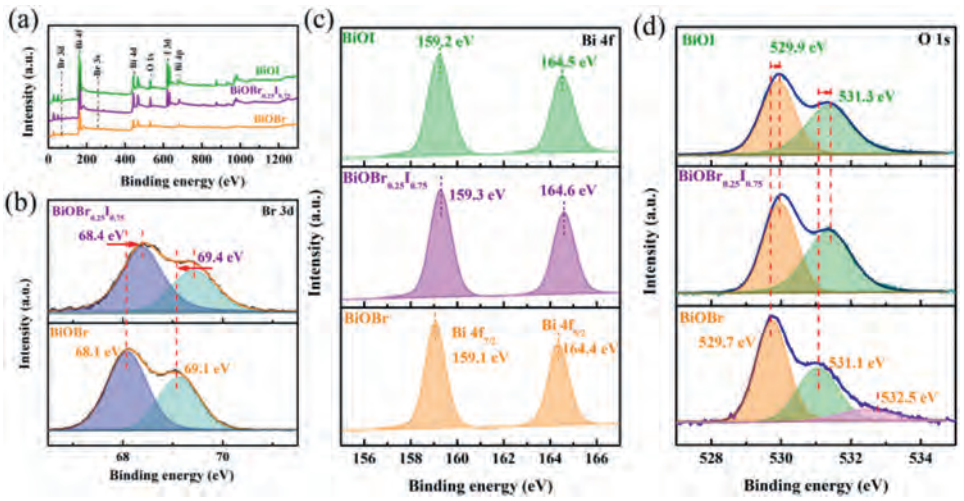

Fig. 4. (a) XPS survey spectra of BiOBr, $BiOBr_{0.25}I_{0.75}$ and BiOI samples. High resolution XPS spectra of (b) Br 3d, (c) Bi 4f and (d) O 1s.

Except for Cr(VI), Cr(III) generated should be pay attention for its potential threat [49]. Fig. 5d shows the concentration variation of total chromium (Cr(T)), Cr(VI) and Cr(III) at pH 2, 5, 7 and 9 by $BiOBr_{0.25}I_{0.75}$. At pH 5, with light illumination, the concentration variations of Cr(T) and Cr(VI) are overlapped. There is no Cr(III) accumulation in solution, indicating that Cr(III) generated by photoreduction process is captured on the surface of $BiOBr_{0.25}I_{0.75}$. The conditions at pH 7 and 9 are the same as pH 5. The variation tendency of Cr(T) and Cr(VI) is overlapped and Cr(III) cannot be detected in solution. That means $BiOBr_{0.25}I_{0.75}$ can effectively capture Cr(III) after photoreduction process. Due to the strong competition of H^+, Cr(III) cannot be immobilized at pH 2. From Fig. 5f, the removal of Cr(T) reaches up to 98% by $BiOBr_{0.25}I_{0.75}$ at pH 4 to 10, indicating $BiOBr_{0.25}I_{0.75}$ is a promising material to remove Cr(T).

The favorable removal of Cr(VI) on $BiOBr_{0.25}I_{0.75}$ can be analyzed from adsorption and photocatalysis performance. The excellent adsorption of Cr(VI) on $BiOBr_{0.25}I_{0.75}$ is caused by its large specific surface area and more mesoporous, which are beneficial for the diffusion of Cr(VI) and the contact of Cr(VI) and photocatalyst. DFT calculations are a better method to analyze the reaction path or calculate the adsorption energy, which has wide application environmental research [50]. To further verify the enhanced adsorption of Cr(VI) on $BiOBr_{0.25}I_{0.75}$, the adsorption energies of Cr(VI) on $BiOBr_{1-x}I_x$ are calculated by DFT calculations. In Fig. 6a, the adsorption energies of Cr(VI) on $BiOBr_{1-x}I_x$ are negative than BiOBr, and the adsorption energy decreases with I content percentage increases, indicating the favorable adsorption capacity. According to previous research, the mechanism for Cr(VI) adsorption is anion exchange between Cr(VI) species ($HCrO_4^-$, CrO_4^{2-}) and X^- (X = Br, I) [29,51,52]. To verify the adsorption mechanism, Fig. 6b shows the concentration variation of Cr(VI), Br^- and I^- at different pH values. From pH 2 to 11, with the decrease of Cr(VI) in solution, the concentration of Br^- and I^- increase, indicating the anion exchange between Cr(VI) species ($HCrO_4^-$, CrO_4^{2-}) and X^- (X = Br, I).

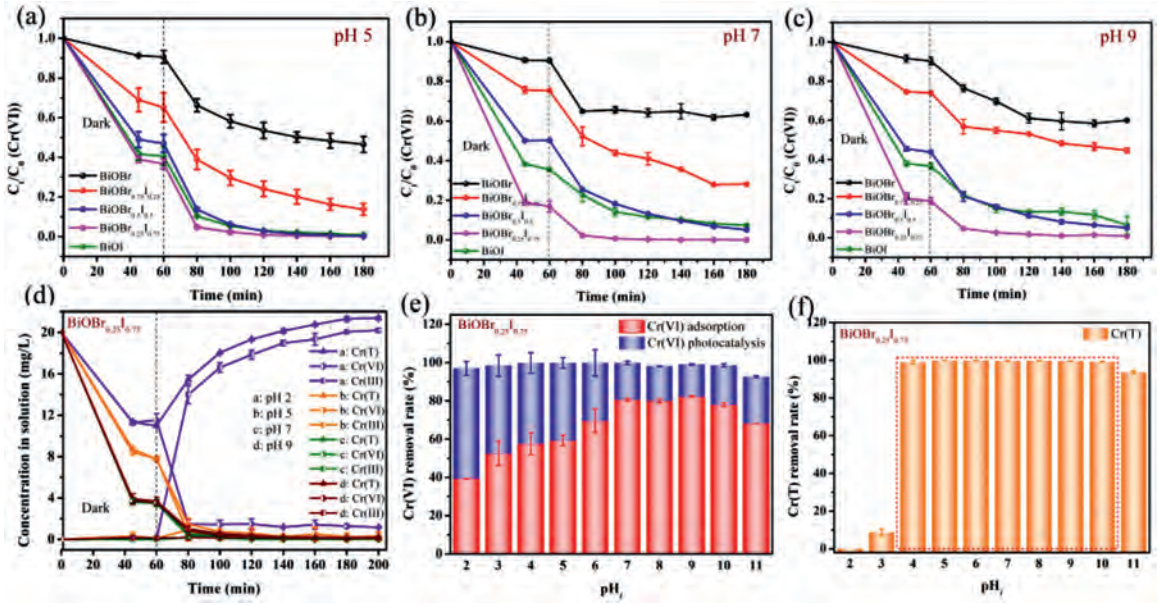

Fig. 5. The adsorption and photoreduction of Cr(VI) by $BiOBr_{1-x}I_x$ at (a) pH 5, (b) pH 7, and (c) pH 9. (d) Removal of Cr(T), Cr(VI) and Cr(III) by $BiOBr_{0.25}I_{0.75}$ at pH 2, 5, 7, 9. (e) Effect of pH_i on the removal of Cr(VI) and (f) Cr(T) by $BiOBr_{0.25}I_{0.75}$. (Experimental conditions: dose of materials, 1 g/L; initial concentration of Cr(VI), 20 mg/L; experiment temperature: 25 °C).

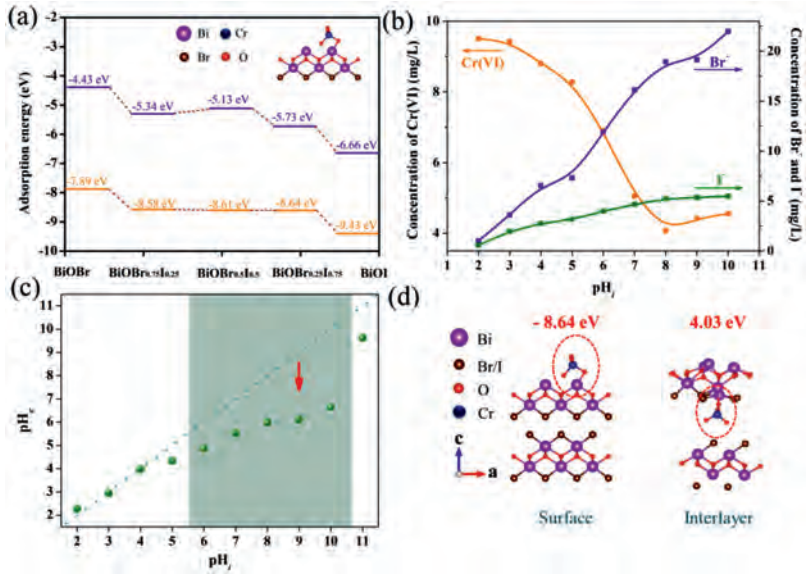

Fig. 6. (a) The adsorption energy of $HCrO_4^-$ and CrO_4^{2-} on $BiOBr_{1-x}I_x$ (the adsorption for $HCrO_4^-$ is in purple and the adsorption for CrO_4^{2-} is in orange). (b) Released Br^- and I^- and remaining Cr(VI) in solution as a function of pH_i. (c) The pH values before and after adsorption. (d) The adsorption energy of CrO_4^{2-} on the surface and interlayer Bi sites.

The pH values after adsorption were detected to further analyze the adsorption process. In Fig. 6c, the pH values decrease after adsorption, which is caused by the anion exchange between OH^- and X^- (X = Br, I). The release of X^- (X = Br, I) facilitates the adsorption of Cr(VI). In order to determine the adsorption site, the adsorption energies of CrO_4^{2-} on $BiOBr_{0.25}I_{0.75}$ were calculated on surface Bi site and interlayer Bi site. In Fig. 6d, the adsorption energies on surface Bi site (−8.64 eV) is much smaller than interlayer Bi site (4.03 eV), thus CrO_4^{2-} will be connected on surface Bi site after anion exchange.

For photoreduction process, the separation and transport efficiency of electrons and holes are very important. The separation and transfer efficiency of electrons and holes were analyzed by electrochemical test and photoluminescence (PL). Fig. 7a shows the visible-light photocurrent responses of BiOBr, $BiOBr_{0.25}I_{0.75}$ and BiOI. With light illumination, $BiOBr_{0.25}I_{0.75}$ presents a distinctly higher current density, about 2-4 times than that of BiOBr and BiOI, which indicates more efficient separation and transfer of photoinduced electrons and holes. Fig. 7b shows the electrochemical impedance of the samples. The model consists of the charge-transfer resistance R_t in parallel with the double-layer capacitance (CPE). The fitting results were calculated on the basis of model in inset in Fig. 7b. The smaller arc radius and R_t (4.360 MΩ) of $BiOBr_{0.25}I_{0.75}$ manifest its higher interfacial charge transfer and separation. The results demonstrate that the introduction of iodine is beneficial for the efficient photogenerated charge carrier separation and transfer. To support of this, PL was conducted

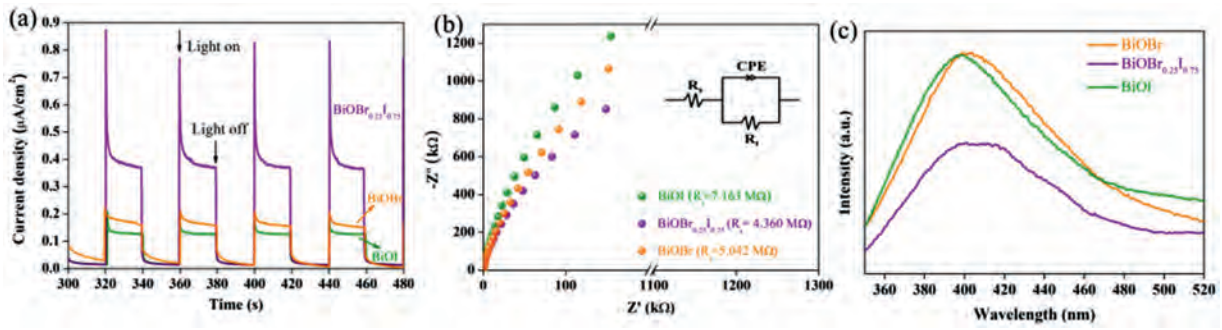

Fig. 7. (a) Transient photocurrent responses, (b) electrochemical impedance spectra, and (c) photoluminescence spectra of BiOBr, $BiOBr_{0.25}I_{0.75}$ and BiOI.

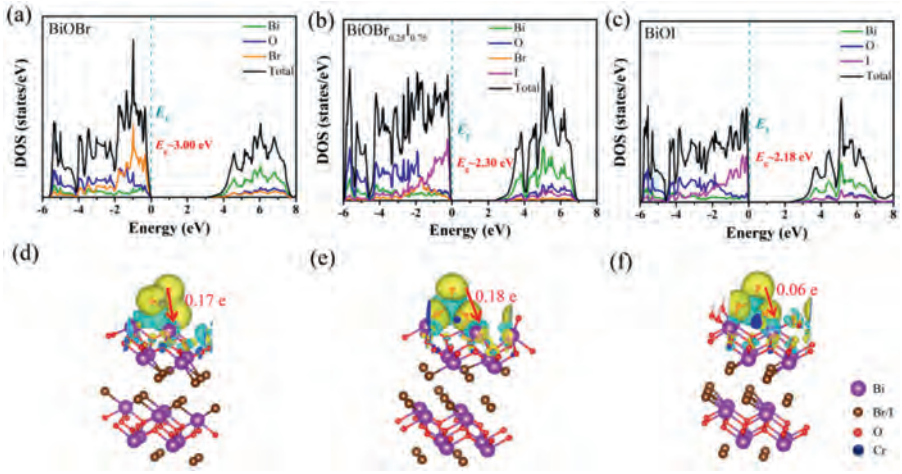

Fig. 8. The calculated electronic density of states of (a) BiOBr, (b) $BiOBr_{0.25}I_{0.75}$, (c) BiOI. Electron density distribution of $BiOBr_{0.25}I_{0.75}$ after CrO_4^{2-} adsorption in (d) acidic, (e) neutral and (f) alkaline conditions (charge accumulation is in yellow and depletion in blue).

to investigate the recombination of electrons and holes (Fig. 7c). Compared with pure BiOBr and BiOI, $BiOBr_{0.25}I_{0.75}$ shows distinct quenching of PL intensity, indicating the lower recombination of electrons and holes. Efficient electrons and holes separation and transfer make more electrons can participate the reduction reaction, thus promoting the photocatalytic reduction of Cr(VI) by $BiOBr_{0.25}I_{0.75}$.

The energy band structure of semiconductor is another factor that affects photoreduction performance, because the position of CB will determine the reduction ability of material, which will influence the efficiency of Cr(VI) removal. In order to verify the contribution of iodine in CB, Figs. 8a-c and Fig. S4 (Supporting information) show the electronic density of states (DOS) of $BiOBr_{1-x}I_x$. For pure BiOBr, the CB consists of Bi 6p and Br 4p orbits. After iodine introducing, the contribution of Br 4p orbit decreases and the contribution of I 5d orbit increases, making the upshift of CBM, enhancing the photoreduction ability. Figs. 8d-f show the electron density distribution of $BiOBr_{0.25}I_{0.75}$ after CrO_4^{2-} adsorption in acidic, neutral and alkaline conditions. The transfer of electrons from CrO_4^{2-} to Bi site can be observed after adsorption, which creates an electron-rich microenvironment, facilitating the reduction process.

Based on our analysis and discussion, Cr(VI) is reduced to Cr(III) within a wide pH range through adsorption and photoreduction. The produced Cr(III) should be immobilized further due to its potential hazard. The highlight of our work is the photoreduciton of Cr(VI) and immobilization of Cr(III) in a wide pH range. To verify the capture of Cr(III), Figs. 9a-d show XPS results of $BiOBr_{0.25}I_{0.75}$ after Cr(VI) photoreduction process, and the process for adsorption and photoreduction of Cr(VI) and immobilization of Cr(III) at different pH values is proposed (Fig. 9e). Different mechanisms lead to different contributions of adsorption and photoreduction. In acidic conditions, photoreduction is the main reason for Cr(VI) removal. At pH 2 and 5, Cr(VI) is reduced to Cr(III) easily, and the generated Cr(III) is adsorbed on the surface of $BiOBr_{0.25}I_{0.75}$ at pH 5, which can be verified by the high resolution of Cr 2p spectrum (Fig. 9b). The peaks at 576.8 and 586.5 eV can be assigned to Cr(III) [53–55]. The negative surface of $BiOBr_{0.25}I_{0.75}$ facilitates the adsorption of Cr(III) through electrostatic attraction (Fig. S5 in Supporting information). With pH increases, the generated and adsorbed Cr(III) decreases from 53.2% to 38.1% (at pH 7) and 39.5% (at pH 9). This is because adsorption is the main reason for Cr(VI) removal under neutral and alkaline conditions (Figs. 9c and d). A small quantity of Cr(VI) are reduced to Cr(III) and captured on the surface of $BiOBr_{0.25}I_{0.75}$. At pH 2, after photoreduction process, there is no Cr(III) accumulation on the surface of $BiOBr_{0.25}I_{0.75}$ due to the strong competition between H^+ and Cr(III) (Fig. 9a). This is not the key point of our research. With the synergy of adsorption, photoreduction and immobilization, we successfully achieve efficient Cr(VI) and Cr(III) removal in a wide pH range.

In summary, the removal of Cr(VI) and immobilization of Cr(III) within a wide pH range are achieved by solid solution $BiOBr_{0.25}I_{0.75}$. The removal mechanism is different at different pH values. Photoreduction is the main reason for Cr(VI) removal under acidic conditions, while adsorption contributes more under neutral and alkaline conditions And $BiOBr_{0.25}I_{0.75}$ can efficiently capture Cr(III) at pH 4 to 10. Our research suggests that $BiOBr_{0.25}I_{0.75}$ is

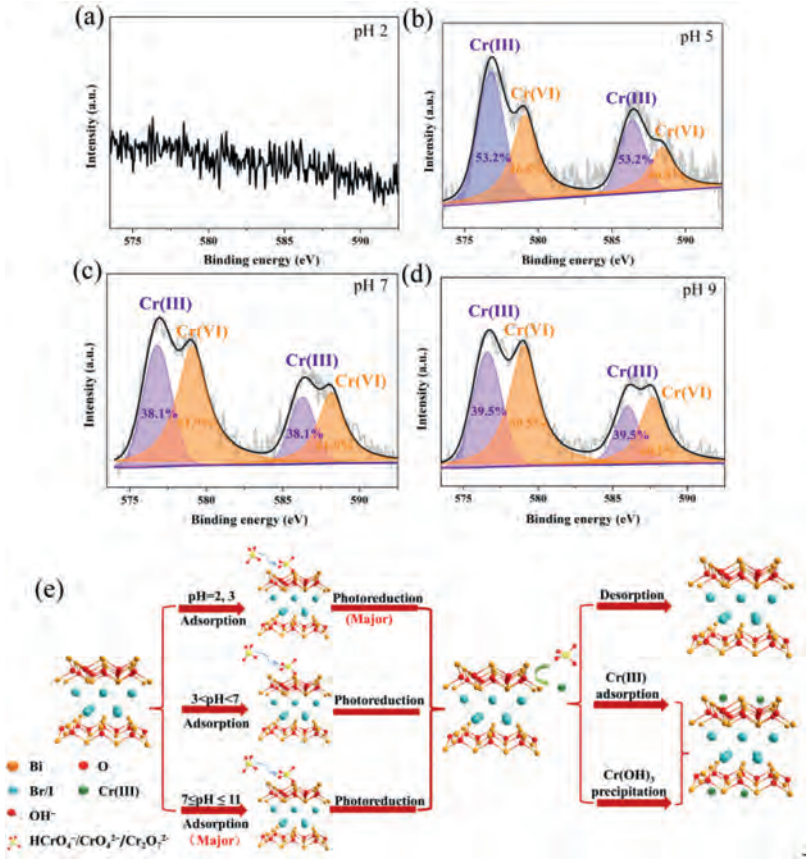

Fig. 9. High resolution of Cr 2p spectrum after photoreduction by $BiOBr_{0.25}I_{0.75}$ at (a) pH 2, (b) pH 5, (c) pH 7, and (d) pH 9. (e) Process for the removal of chromium on $BiOBr_{0.25}I_{0.75}$

a potential material for water treatment, especially for chromium-containing wastewater in a wide pH range.

Declaration of competing interest

The authors declare that they have no known competing financial interests or personal relationships that could have appeared to influence the work reported in this paper.

Acknowledgments

This work was supported by the Natural Science Foundation of Tianjin (No. 18JCYBJC17700), the National Natural Science Foundation of China (Nos. 21406164, 21466035 and 22066022).

Supplementary materials

Supplementary material associated with this article can be found, in the online version, at doi:10.1016/j.cclet.2021.09.043.

References

[1] D. Wang, Y. Xu, L. Jing, et al., J. Hazard. Mater. 384 (2020) 121480–121489.
[2] A. Jin, X. Liu, M. Li, et al. , ACS Sustain. Chem. Eng. 7 (2019) 5122–5133.
[3] A. Zhitkovich , Chem. Res. Toxicol. 24 (2011) 1617–1629.
[4] Y. Liu, Z. Shen, J. Song, et al. , Chin. Chem. Lett. 31 (2020) 2747–2751.
[5] M. Sun, F. Li, M. Su, et al., J. Colloid Interface Sci. 596 (2021) 278–287.
[6] H.H. Wu, C.W. Chang, D. Lu, et al. , ACS Appl. Mater. Interfaces 11 (2019) 35702–35712.
[7] B.A. Marinho, R. Djellabi, R.O. Cristóvão, et al., Chem. Eng. J. 318 (2017) 76–88.
[8] Y. Wang, L. Rao, P. Wang, et al., Appl. Catal. B: Environ. 262 (2020) 118308.
[9] F. Chen, M. Zhang, L. Ma, et al., Sci. Total Environ. 730 (2020) 138930.
[10] H. Shen, F. Fu, W. Xue, et al., J. Colloid Interface Sci. 599 (2021) 741–751.
[11] B. Valizadeh, T.N. Nguyen, S. Kampouri, et al. , J. Mater. Chem. A 8 (2020) 9629–9637.
[12] Z. Ding, J. Liang, W. Zhang, et al. , J. Mater. Chem. A 8 (2020) 11362–11369.
[13] W. Chen, Z. Yang, Z. Xie, et al. , J. Mater. Chem. A 7 (2019) 998–1004.
[14] S. Wang, X. Zhao, H.M.A. Sharif, et al., Chem. Eng. J. 406 (2021) 126849.
[15] R. Yuan, C. Yue, J. Qiu, et al., Appl. Catal. B: Environ. 251 (2019) 229–239.
[16] F. Li, Z. Wei, K. He, et al., Water Res. 185 (2020) 116219.
[17] W. Liu, J. Ni, X. Yin, Water Res. 53 (2014) 12–25.
[18] N. Li, Y. Tian, J. Zhao, et al., Appl. Catal. B: Environ. 214 (2017) 126–136.
[19] L. Jiang, Y. Xie, F. He, et al. , Chin. Chem. Lett. 32 (2021) 2187–2191.
[20] Z. Shi, Y. Zhang, G. Duoerkun, et al. , Environ. Sci. Nano 7 (2020) 2708–2722.
[21] S.M. El-Sheikh, A.B. Azzam, R.A. Geioushy, et al., J. Alloys Compd. 857 (2021) 157513–157524.
[22] Z. Chen, J. Zhao, J. Chen, et al., Sep. Purif. Technol. 258 (2021) 118007.
[23] C. Zhao, J. Wang, X. Chen, et al., Sci. Total Environ. 752 (2021) 141901.
[24] J. Di, J. Xia, M. Ji, et al. , J. Mater. Chem. A 3 (2015) 15108–15118.
[25] Y. Bai, L. Ye, T. Chen, et al., Appl. Catal. B: Environ. 203 (2017) 633–640.
[26] L. Meng, Y. Qu, L. Jing, Chin. Chem. Lett. (2021), doi:10.1016/j.cclet.2021.03.083.
[27] J. Shang, W. Hao, X. Lv, et al. , ACS Catal. 4 (2014) 954–961.
[28] Z. Long, G. Zhang, H. Du, et al., J. Hazard. Mater. 407 (2021) 124394.
[29] L. Jia, W. Zhou, X. Huang, et al. , Environ. Sci. Nano 6 (2019) 3601–3610.
[30] J. Wu, Y. Xie, Y. Ling, et al., Chem. Eng. J. 400 (2020) 125944.
[31] J.E.D. Davies, J. Inorg , Nucl. Chem. 35 (1973) 1531–1534.
[32] W. Zeng, J. Li, L. Feng, et al. , Adv. Funct. Mater. 29 (2019) 1900129.
[33] W.L. Huang , J. Comput. Chem. 30 (2009) 1882–1891.
[34] W.L. Huang, Q. Zhu , Comput. Mater. Sci. 43 (2008) 1101–1108.
[35] T. Jia, J. Wu, J. Song, et al., Chem. Eng. J. 396 (2020) 125258.
[36] S. Chen, D. Huang, G. Zeng, et al., Chem. Eng. J. 382 (2020) 122840.
[37] X. Xue, R. Chen, H. Chen, et al. , Nano Lett. 18 (2018) 7372–7377.
[38] Q. Wang, Z. Liu, D. Liu, et al., Appl. Catal. B: Environ. 236 (2018) 222–232.
[39] G. Zhang, D. Chen, N. Li, et al., Appl. Catal. B: Environ. 250 (2019) 313–324.
[40] J. Bai, J. Sun, X. Zhu, et al. , Small 16 (2020) 1904783.
[41] J. Qi, J. Liu, F. Sun, et al., Chin. Chem. Lett. 32 (2021) 1814–1818.
[42] L. Li, L. Ai, C. Zhang, et al. , Nanoscale 6 (2014) 4627–4634.
[43] X. Wu, K. Zhang, G. Zhang, et al., Chem. Eng. J. 325 (2017) 59–70.
[44] N. Liu, C. Schneider, D. Freitag, et al. , Nano Lett. 14 (2014) 3309–3313.
[45] C. Mao, H. Cheng, H. Tian, et al., Appl. Catal. B: Environ. 228 (2018) 87–96.
[46] Y. Yu, K. Wu, W. Xu, et al. , J. Hazard. Mater. 404 (2021) 124171.
[47] X. Wang, S.O. Pehkonen, A.K. Ray, Ind. Eng. Chem. Res. 43 (2004) 1665–1672.

[48] H. Liang, T. Li, J. Zhang, et al., J. Colloid Interface Sci. 558 (2020) 85–94.
[49] R. Li, D. Hu, K. Hu, et al., Sci. Total Environ. 704 (2020) 135284.
[50] M. Ma, L. Chen, J. Zhao, et al., Chin. Chem. Lett. 30 (2019) 2191–2195.
[51] T. Li, Y. Gao, L. Zhang, et al., Appl. Catal. B: Environ. 277 (2020) 119065–119074.
[52] T. Li, G. Zhang, H. Lan, et al. , ACS Sustain. Chem. Eng. 7 (2019) 2429–2436.
[53] R.A. Geioushy, S.M. El-Sheikh, A.B. Azzam, et al., J. Hazard. Mater. 381 (2020) 120955.
[54] C. Zhu, F. Liu, L. Song, et al., Environ. Sci. Nano 5 (2018) 487–496.
[55] Y. Yang, J. Li, T. Yan, et al., J. Colloid Interface Sci. 562 (2020) 493–501.